Kinematic and highly reduced-dynamic LEO orbit determination for gravity field estimation

A. Jäggi, G. Beutler, H. Bock, U. Hugentobler
Astronomical Institute,
University of Bern, Sidlerstrasse 5, CH-3012 Bern, Switzerland
email: adrian.jaeggi@aiub.unibe.ch

Abstract. Kinematic positions of low Earth orbiting satellites equipped with spaceborne GPS receivers are widely used as input for subsequent gravity field estimation procedures. Positions relying on reduced-dynamic orbit determination, however, are often considered as inappropriate for this task, because they depend to some extent on the gravity field model underlying the orbit estimation. We review the principles of reduced-dynamic orbit determination and give the mathematical background for a very efficient estimation scheme of reduced-dynamic satellite trajectories using least-squares methods. Simulated as well as real data from the CHAMP GPS receiver are used to show the equivalence of kinematic and reduced-dynamic orbits in the kinematic limit and to present a highly reduced-dynamic orbit determination scheme as an alternative to kinematic point positioning.

Key words. Low Earth orbiter, reduced-dynamic orbit determination, kinematic orbit determination

1 Introduction

A new era in using data from spaceborne GPS receivers on board low Earth orbiters (LEOs) for gravity field determination was opened in the framework of the CHAMP mission (Reigber *et al*., 2002). The combined analysis of high-low GPS satellite-to-satellite tracking data and STAR accelerometer data (Touboul *et al*., 1999) enabled the derivation of a whole series of high quality global gravity field models with unprecedented accuracy (see, e.g., Reigber *et al*., 2003).

Due to the heavy demands posed on computational resources in the case of classical numerical integration techniques, alternative methods have been developed and established as well, e.g., relying on satellite positions used as pseudo-observables (see, e.g., Visser *et al*., 2003). Gerlach *et al*. (2003) used kinematic CHAMP positions, which were precedingly derived by Švehla and Rothacher (2003), as pseudo-observations together with accelerometer data and showed that gravity field models can be estimated with a quality comparable to the official CHAMP models by means of the energy integral method. Gerlach *et al*. (2003) reported that gravity field models derived from reduced-dynamic orbits (RD-orbits) are biased towards the a priori gravity field model used for the preceding orbit estimation.

This article focuses on both reduced-dynamic and kinematic precise orbit determination (POD) for the purpose of gravity field estimation. We analyze so-called highly RD- (HRD-) and maximum RD-orbits (MRD-orbits) as alternatives to kinematic orbits. Simulated and real GPS data of the CHAMP receiver are used to investigate the properties of such orbits and to assess their value for a subsequent gravity field estimation, where the main issue consists of clarifying dependencies of orbital positions and velocities on the a priori gravity field models used.

2 LEO orbit determination

This section briefly introduces kinematic, dynamic and reduced-dynamic orbit modelling techniques applied to LEOs equipped with on board GPS receivers. The main focus lies on a brief review of a novel approach proposed by Beutler *et al*. (2005) for a very efficient computation of any type of RD-orbits. RD-orbit modelling techniques are of particular interest because they contain the two other above mentioned techniques as special (asymptotic) cases.

2.1 Kinematic orbit determination

The geometric strength and the high density of GPS observations allows for a purely geometrical approach to determine LEO positions at the observation epochs by precise point positioning (Švehla and Rothacher, 2004). The ephemeris are represented by a time series of three kinematic coordinates per kinematic epoch, which are determined in a standard least-squares adjustment process of GPS observations together with all other relevant parameters without using any information on LEO dynamics.

2.2 Dynamic orbit determination

The equation of motion of an Earth orbiting satellite including all perturbations reads in the inertial frame

as

$$\ddot{\boldsymbol{r}} = -GM\frac{\boldsymbol{r}}{r^3} + \boldsymbol{f}_1(t, \boldsymbol{r}, \dot{\boldsymbol{r}}, q_1, ..., q_d) \tag{1}$$

with a set of initial conditions $\boldsymbol{r}^{(k)}(t_0) = \boldsymbol{r}^{(k)}(E_1, ..., E_6; t_0)$, $k = 0, 1$ where $E_1, ..., E_6$ are the six Keplerian elements pertaining to epoch t_0. $q_1, ..., q_d$ denote d additional dynamical parameters considered as unknowns, which describe the perturbing acceleration acting on the satellite.

Let us assume that an a priori orbit $\boldsymbol{r}_0(t)$ is available, e.g., from a GPS code solution. Dynamic orbit determination may then be set up as an orbit improvement process, i.e., the actual orbit $\boldsymbol{r}(t)$ is expressed as a truncated Taylor series with respect to the unknown orbit parameters p_i about the a priori orbit, which is represented by the parameter values p_{i0}:

$$\boldsymbol{r}(t) = \boldsymbol{r}_0(t) + \sum_{i=1}^{n} \frac{\partial \boldsymbol{r}_0(t)}{\partial p_i} \cdot \Delta p_i \ , \tag{2}$$

where $\Delta p_i \doteq p_i - p_{i0}$ denote the $n \doteq 6 + d$ corrections to be estimated. Numerical integration techniques must usually be applied to solve the so-called variational equations (see, e.g., Beutler, 2004) to obtain the partial derivatives of the a priori orbit $\boldsymbol{r}_0(t)$ with respect to the parameters p_i, which allow the solution for the corrections Δp_i in a standard least-squares adjustment process of GPS observations together with all other relevant parameters. Eventually, the improved orbit may be computed according to Eq. (2). As the obtained orbit is a particular solution of the equation of motion, the trajectory fully depends on the dynamical model defined by Eq. (1).

2.3 Reduced-dynamic orbit determination

We use pseudo-stochastic orbit modelling techniques (Jäggi *et al*., 2005) as a realization for RD-POD (Wu *et al*., 1991), which makes use of both the geometric strength of the GPS observations and the fact that satellite trajectories are particular solutions of an equation of motion. The attribute "pseudo" is used to distinguish our approach from methods considering the satellite motion as a stochastic process, whereas the attribute "stochastic" refers to the introduction of additional parameters to the deterministic equation of motion, which may have a priori known statistical properties. In this article we make use of two types of additional parameters, namely instantaneous velocity changes (pulses) and piecewise constant accelerations.

2.3.1 Instantaneous velocity changes

Pulses are attractive for RD LEO POD mainly because a large number of pulses can be set up efficiently. This is due to the fact that a pulse-induced orbital change may be expressed only by a change in the Keplerian elements (see, e.g., Jäggi *et al*., 2004a). Therefore, the partial derivative of the a priori orbit with respect to a pulse v_{ij} at time t_i in direction j, subsequently denoted as $\boldsymbol{z}_{v_{ij}}$, may be expressed as a linear combination of the partial derivatives with respect to the initial conditions $E_1, ..., E_6$:

$$\boldsymbol{z}_{v_{ij}}(t) = \begin{cases} \boldsymbol{0} & ; t < t_i \\ \sum\limits_{k=1}^{6} \beta_{ij,k} \cdot \boldsymbol{z}_{E_k}(t) & ; t \geq t_i \end{cases} . \tag{3}$$

Independent of the number of pseudo-stochastic pulses set up, only the six variational equations referring to the initial conditions have to be integrated numerically to subsequently compute all partial derivatives with respect to the pulses as simple linear combinations with constant coefficients.

2.3.2 Piecewise constant accelerations

Piecewise constant accelerations are attractive for RD LEO POD, as well, because a large number of accelerations can be set up efficiently, as well. Jäggi *et al*. (2004a) showed that the partial derivative of the a priori orbit with respect to an acceleration a_i acting in the subinterval $t_{i-1} \leq t < t_i$ in direction j may be written as a linear combination with time-dependent coefficients of the partial derivatives with respect to the initial conditions $E_1, ..., E_6$:

$$\boldsymbol{z}_{a_{ij}}(t) = \begin{cases} \boldsymbol{0} & ; t < t_{i-1} \\ \sum\limits_{k=1}^{6} \beta_{ij,k}(t) \cdot \boldsymbol{z}_{E_k}(t) & ; t_{i-1} \leq t < t_i \\ \sum\limits_{k=1}^{6} \beta_{ij,k}(t_i) \cdot \boldsymbol{z}_{E_k}(t) & ; t \geq t_i \end{cases} , \tag{4}$$

or, alternatively, as a linear combination with constant coefficients of the same partial derivatives and one additional partial derivative with respect to a constant acceleration pointing in the same direction and acting over the entire orbital arc. Therefore, all partial derivatives with respect to the accelerations may be constructed from a very limited set of numerically integrated partial derivatives.

2.3.3 Normal equation system

We give a short overview of the structure of the resulting normal equation system for the standard least-squares adjustment process of GPS observations. For the sake of simplicity, we consider only the six orbital elements and the pulses in three orthogonal directions at times t_i, $i = 1, ..., n-1$ as parameters. For a more detailed derivation, also considering different parameter types like piecewise constant accelerations and

additional parameter types like carrier phase ambiguities, we refer to Beutler *et al*. (2005).

The pulse-epochs divide the orbital arc into n subintervals. Let us write all n_{o_i} observation equations of the subinterval $I_i = [t_i, t_{i+1})$ in a convenient matrix notation:

$$\boldsymbol{A}_i \cdot \boldsymbol{\Delta E} + \boldsymbol{A}_i \cdot \sum_{m=1}^{i} \boldsymbol{B}_m \cdot \boldsymbol{\Delta v}_m - \boldsymbol{\Delta \phi}_i = \boldsymbol{\rho}_i \ , \tag{5}$$

where $\boldsymbol{A}_i$ is the first design matrix with n_{o_i} lines and six columns, $\boldsymbol{\Delta E}$ the column array containing the six increments of the initial osculating elements, $\boldsymbol{B}_{i[k,j]} = \beta_{ij,k}$ the matrix with six lines and three columns containing the coefficients of Eq. (3), $\boldsymbol{\Delta v}_i$ the column array containing the three pulses at time t_i, $\boldsymbol{\Delta \phi}_i$ the column array containing the n_{o_i} terms "observed-computed", and $\boldsymbol{\rho}_i$ the column array containing the n_{o_i} residuals. Note that all pulses set up before the subinterval I_i remain active and contribute to the observation equations of subinterval I_i as predicted by the linear combination of Eq. (3). Therefore, the last subinterval eventually contains the contributions due to all pulses of the orbital arc, provided that the initial conditions are still referring to the beginning of the orbital arc.

To study the structure of the resulting normal equation matrix, it is instructive to use the contributions $\boldsymbol{N}_i \doteq \boldsymbol{A}_i^T \boldsymbol{P}_i \boldsymbol{A}_i$ per subinterval to the normal equation matrix of dynamic POD, i.e., POD without pulses. Obviously, these contributions form the complete normal equation matrix of dynamic POD as $\boldsymbol{N} \doteq \sum_{i=0}^{n-1} \boldsymbol{A}_i^T \boldsymbol{P}_i \boldsymbol{A}_i$, but they are also the building blocks of the complete, symmetric normal equation matrix in the presence of pulses, which reads as

$$\begin{pmatrix} \boldsymbol{N} & \sum\limits_{i=1}^{n-1} \boldsymbol{N}_i \boldsymbol{B}_1 & \cdots & \sum\limits_{i=n-1}^{n-1} \boldsymbol{N}_i \boldsymbol{B}_{n-1} \\ . & \boldsymbol{B}_1^T \sum\limits_{i=1}^{n-1} \boldsymbol{N}_i \boldsymbol{B}_1 & \cdots & \boldsymbol{B}_1^T \sum\limits_{i=n-1}^{n-1} \boldsymbol{N}_i \boldsymbol{B}_{n-1} \\ . & . & \ddots & \vdots \\ . & . & . & \boldsymbol{B}_{n-1}^T \sum\limits_{i=n-1}^{n-1} \boldsymbol{N}_i \boldsymbol{B}_{n-1} \end{pmatrix} . \tag{6}$$

Equation (6) illustrates that the normal equation matrix (and also the corresponding right hand side of the normal equation system) has a simple structure, but grows monotonically after having processed all observations of one subinterval. Note in particular that it is not possible to pre-eliminate the pulses at any observation epoch which is indicated by the upper summation limit. Beutler *et al*. (2005) made full use of the structure of Eq. (6) and found that for a large variety of applications the solution vector and the associated full variance-covariance information may be computed with sufficient efficiency. However, when striving to the kinematic limit, i.e., pseudo-stochastic parameters set up at a rate close or equal to the observation sampling rate, the procedures become inefficient due to the unavoidably large normal equation matrix, which has to be inverted.

2.3.4 Transformation of Keplerian elements

Rearranging all observation equations (Eq. (5)) of the subinterval I_i shows that the orbit may be represented within this subinterval by only six Keplerian elements:

$$\boldsymbol{A}_i \cdot \left(\boldsymbol{\Delta E} + \sum_{m=1}^{i} \boldsymbol{B}_m \cdot \boldsymbol{\Delta v}_m \right) - \boldsymbol{\Delta \phi}_i = \boldsymbol{\rho}_i \ , \tag{7}$$

where the term in parentheses denotes the column array containing the six orbital elements pertaining to epoch t_0, but characterizing the trajectory within this particular subinterval. This set of elements, subsequently denoted as $\boldsymbol{\Delta E}_i$, is simply related to the set of elements of the previous subinterval by:

$$\boldsymbol{\Delta E}_i = \boldsymbol{\Delta E}_{i-1} + \boldsymbol{B}_i \cdot \boldsymbol{\Delta v}_i \ . \tag{8}$$

It is instructive to apply the transformation given in Eq. (8) each time after having processed all observations of one subinterval. The resulting normal equation matrix then reads as:

$$\begin{pmatrix} \boldsymbol{N} & -\sum\limits_{i=0}^{0} \boldsymbol{N}_i \boldsymbol{B}_1 & \cdots & -\sum\limits_{i=0}^{n-2} \boldsymbol{N}_i \boldsymbol{B}_{n-1} \\ . & \boldsymbol{B}_1^T \sum\limits_{i=0}^{0} \boldsymbol{N}_i \boldsymbol{B}_1 & \cdots & \boldsymbol{B}_1^T \sum\limits_{i=0}^{0} \boldsymbol{N}_i \boldsymbol{B}_{n-1} \\ . & . & \ddots & \vdots \\ . & . & . & \boldsymbol{B}_{n-1}^T \sum\limits_{i=0}^{n-2} \boldsymbol{N}_i \boldsymbol{B}_{n-1} \end{pmatrix} . \tag{9}$$

The solution vector obtained from the transformed normal equation system contains the same pulses as the untransformed system, but the set of elements $\boldsymbol{\Delta E}_{n-1}$ referring to the last subinterval (instead of $\boldsymbol{\Delta E}_0$ referring to the first subinterval). A comparison with the untransformed normal equation matrix (compare Eq. (6)) reveals the benefit of the applied transformation because it is now possible to pre-eliminate the pulses after each subinterval as the upper summation limits in Eq. (9) indicate. Beutler *et al*. (2005) made full use of the structure of Eq. (9) and proposed a very efficient pre-elimination and back-substitution scheme for different types of pseudo-stochastic parameters, which allows it to efficiently realize the kinematic limit with RD-orbits.

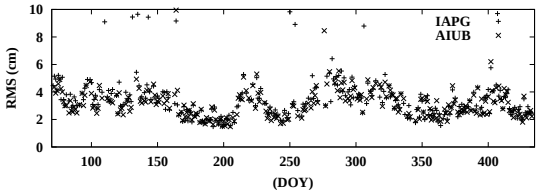

Fig. 1. Daily (1-dim.) RMS of differences for AIUB kinematic and IAPG kinematic orbits w.r.t. conventional RD-orbits for days 071/2002 to 070/2003.

3 Processing of real CHAMP data

The GPS final orbits and the 30 s high-rate satellite clock corrections from the CODE analysis center were used together with attitude data from the star tracker on board of CHAMP provided by GFZ (GeoForschungsZentrum Potsdam) and the gravity field model EIGEN-2 (Reigber *et al*., 2003) to conventionally process undifferenced CHAMP GPS phase tracking data covering a one year time period from day 071/2002 to 070/2003. For a subset of tracking data, covering GPS weeks 1173-1176, 10 s GPS satellite clock corrections were generated in order to perform tests with several kinds of HRD orbit parametrization. All computations were performed with a development version of the Bernese GPS Software (Hugentobler *et al*., 2001).

3.1 Results of kinematic POD

Figure 1 shows daily (1-dim.) RMS values of orbital differences derived from our kinematic orbits (AIUB) with respect to conventional RD-orbits with pseudo-stochastic parameters set up every six minutes. As a reference, the differences emerging from the kinematic orbits (IAPG) computed by Švehla and Rothacher (2003) are displayed as well. The two curves show, on the one hand, that both sets of kinematic orbits are of similar quality, but, on the other hand, they reveal for both solutions a considerable number of poorly determined trajectories, mainly due to data quality issues. As a consequence of the very low degree of freedom per epoch, kinematic positions react very sensitively to the density and quality of GPS observations. This makes a robust preprocessing a greater challenge than for conventional RD-POD.

3.2 RD-POD at the kinematic limit

The estimation scheme presented in section 2.3.4 makes it possible to efficiently approach the kinematic limit with RD-orbits. For one particular day Fig. 2 (top) puts the cross-track differences for the kinematic orbit together with the differences emerging from two HRD-orbits, i.e., orbits which are represented by six initial conditions and three unconstrained pulses set up every one and every three minutes, respectively. We see that the HRD-orbits approach the kinematic orbit when the number of pulses increases. Because the differences for the MRD-orbit would completely overlap with the differences for the kinematic orbit, Fig. 2 (bottom) displays the differences between both orbits separately and confirms their equivalence to the numerical precision provided by the SP3 orbit file format, apart from a few exceptions which are discussed in the following paragraph.

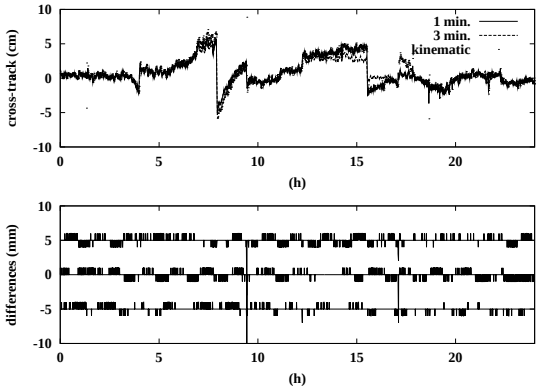

Fig. 2. Cross-track differences of the kinematic and different HRD-orbits w.r.t. a conventional RD-orbit (top) and differences (radial/cross-track shifted by 5 mm) between the kinematic and the MRD-orbit (bottom) for day 198/2002.

3.2.1 Properties of MRD-orbits

The least-squares adjustment process for the estimation of a MRD-orbit, either based on pulses or accelerations, results in a regular normal equation system like in the case of kinematic POD. It is instructive to have a closer look at MRD-orbits in order to emphasize possible benefits of HRD-orbits. For the sake of simplicity we confine ourselves to discuss the results achieved with pulses, because MRD-orbits based on accelerations do not provide more insight in this respect.

For MRD-orbits, three unconstrained pulses are set up at all n_{obs} observation epochs, except for the very first and the very last one. Therefore, together with the six initial conditions, a total number of $3 \cdot n_{obs}$ orbit parameters are estimated, which is obviously the same number of unknowns as in the case of a kinematic orbit. Provided that at least four GPS observations are available for every observation epoch, all epoch parameters can be determined for both approaches, i.e., three pulses and three kinematic coordinates, respectively, and a receiver clock correction. Both orbit ephemeris are equivalent at the observation epochs as illustrated in Fig. 3 (top).

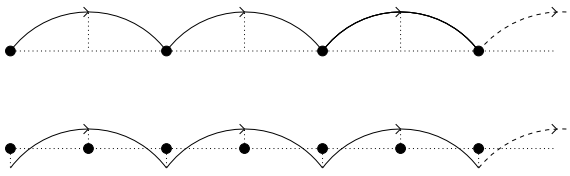

Fig. 3. MRD-orbit (solid line) based on pulses in comparison with the true orbit (dotted line) (top) and impact of an increased sampling rate (bottom).

The trajectory of the MRD-orbit is defined in-between the observation epochs, as well. The positions at the left and at the right boundary epochs provide the necessary six conditions to define a trajectory between these two points, which solves the equation of motion (Eq. (1)). Note that the positions at the observation epochs are completely independent of the force field, but the trajectory in-between and in particular the orbital velocity is given by the a-priori force model. It is thus not possible to derive more independent information concerning the force field from a MRD-orbit than from a kinematic orbit. The same statement holds if accelerations are set up with the highest possible resolution, where the trajectory in-between is allowed to have large excursions ("slalom"-orbit).

If there are less than four GPS observations available at a certain epoch, it is not possible to estimate all three pulses. Figure 2 (bottom) includes such epochs where the filtering due to the dynamic orbit model starts to affect the MRD-trajectory, which is responsible for a few larger differences. A closer inspection shows that this effect is limited to the neighboring epochs of intervals with few observations. For a few days, however, we also found deviations lasting longer, a case to be investigated further.

3.2.2 Properties of HRD-orbits

Section 3.2.1 showed that MRD-orbits may be considered as equivalent to kinematic orbits. In order to make use of filtering effects associated with RD-orbits, it is thus necessary to set up pseudo-stochastic parameters at subintervals of length T_p longer than the observation sampling interval T_s. Because T_p determines, in essence, the achievable resolution for a subsequent gravity field recovery procedure, T_s should be rather decreased than T_p increased. Figure 3 (bottom) illustrates this for pulses in comparison to the case of maximum resolution (top). The trajectory is filtered with the force model because $T_s < T_p$, which leads to a trajectory with a reduced scatter. As a drawback, however, the results show a dependency on the force model as illustrated in Fig. 3 (bottom), even if the orbital positions are evaluated only at the pulse epochs. A simulation study in section 4 is used to establish the relationship between the additional force field dependency and the reduction of noise.

Table 1. Overall RMS of velocity differences w.r.t. conventional RD-orbits (GPS weeks 1173-1176).

Solution	30s GPS-sampling (mm/s)	10s GPS-sampling (mm/s)
kinematic	0.19	0.23
30s pulses	(0.15)	0.24
30s acc.	(9.26)	0.30
60s pulses	0.14	0.15
60s acc.	0.17	0.15

3.3 Results of HRD-POD

Commonly used gravity field recovery procedures do not only use the orbital positions as pseudo-observables. The energy integral method, e.g., requires instantaneous orbital velocities to compute disturbing potential values along the orbit (Földváry *et al.*, 2004). Table 1 gives an impression of the scatter of four weeks of CHAMP orbital velocities obtained for different solutions with respect to conventional RD-orbit velocities. The solutions in parentheses (e.g., the "slalom"-orbit, see section 3.2.1) have no value for gravity field recovery and are listed just for completeness. In general, we recognize that pulse-based solutions show a smaller RMS than acceleration-based solutions for high resolutions, but would encounter an opposite behavior if the resolution was further decreased. We have to keep in mind, however, that a small noise for pulse-based solutions does not necessarily indicate a better qualification for gravity field recovery, e.g., due to dependencies on the a priori gravity field model.

The results listed in Table 1 are in good agreement with the expectations from the simulation study following in section 4, with two exceptions. First, the 10 s kinematic velocities are slightly noisier than the 30 s based velocities, even if the same 7-point Newton-Gregory interpolation was applied to the kinematic positions (Földváry *et al.*, 2004). This might indicate a problem with the 10 s GPS satellite clock corrections, in particular because an almost identical RMS of 0.20 mm/s results, if the velocities are evaluated every 30 s only. Secondly, simulated data predict only a slightly larger RMS for 30 s acceleration-based velocities with 10 s sampling than for the 10 s kinematic velocities. This prediction is not confirmed by the observed RMS of 0.30 mm/s and needs to be investigated further.

4 Simulation study

A 24 h dynamic CHAMP orbit in a true gravity field, defined by the gravity field model EIGEN-2 up to degree and order 120, served as the true orbit to sim-

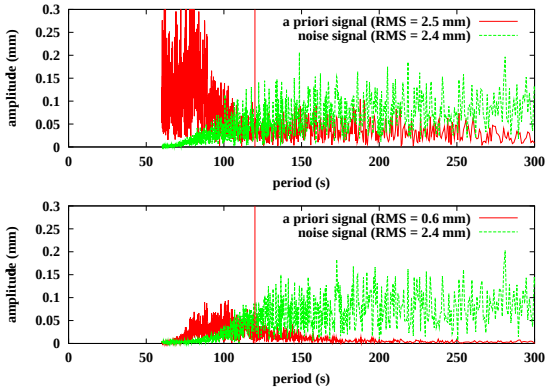

Fig. 4. Amplitude spectra due to noise and due to force model errors for HRD-orbit positions based on pulses (top) and accelerations (bottom) with T_s = 30 s and T_p = 60 s.

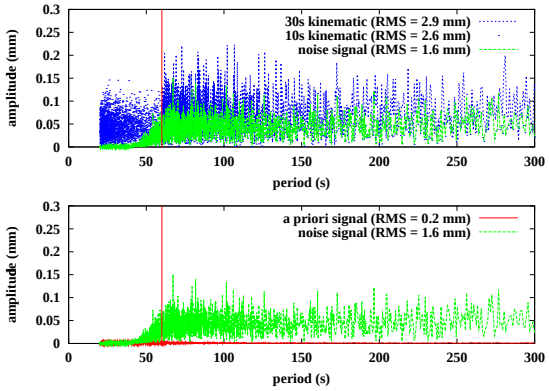

Fig. 5. Noise spectra (top) for 10 s and 30 s kinematic orbits and HRD-orbit based on accelerations with T_s = 10 s and T_p = 30 s and spectrum due to force model errors (bottom).

ulate undifferenced GPS phase observations, which were generated either free of noise or, alternatively, with a white noise of 1 mm RMS error. A different a priori gravity field model was then used to reconstruct the true orbit with different POD strategies. Eventually, Fourier analysis techniques were used to study the differences of the estimated orbital positions and velocities with respect to the true values in the frequency domain. A rather poor a priori gravity field, realized by the EIGEN-2 model truncated at degree and order 20, was used to reconstruct the true orbits. In addition, the low degree and order spherical harmonic coefficients (≤ 20) were slightly modified according to the formal error estimates provided by the EIGEN-2 model.

4.1 Fourier analysis of orbital positions

Figure 4 shows amplitude spectra of orbital position differences over one day emerging from HRD-orbits based on pulses (top) and accelerations (bottom), respectively, with T_s = 30 s and T_p = 60 s. The amplitude spectra denoted as 'a priori signal' characterize the residual impact of the a priori gravity field model in a noise-free simulation. The amplitude spectra denoted as 'noise signal' characterize the impact of the 1 mm GPS phase observation noise in absence of any gravity field model errors. Fig. 4 confirms, in essence, that orbit difference signals with periods $T < 2 \cdot T_p$ (indicated by a vertical line in all spectra) are dominated by the a priori gravity field model as the a priori gravity field induced signal amplitudes exceed the apparent amplitudes caused by the observation noise, which is strongly reduced in the highest frequency range due to the RD-filtering. The effect illustrated in Fig. 3 (bottom), however, explains that the impact of the a priori gravity field model is not only restricted to periods $T < 2 \cdot T_p$ as one might expect from an ideal filter, but also leaks into the lower frequency range. It is in particular possible for RD-orbits based on pulses and larger values of T_p that the signal spectrum exceeds the noise spectrum also for few periods larger than $2 \cdot T_p$. As expected, accelerations show a slightly better noise reduction and a greatly reduced dependency on the a priori gravity field model over the entire frequency range, because the unexplained gravity field signal is not only absorbed at certain discrete epochs.

Figure 5 shows analogue spectra for the more interesting case with T_s = 10 s and T_p = 30 s based on accelerations. Figure 5 (bottom) indicates a negligible influence of the a priori gravity field signal in comparison to the noise level, at least over the considered one-day time interval (see section 4.3). Figure 5 (top) also shows the noise spectra of 10 s and 30 s kinematic orbits. Taking into account that the level of the last mentioned spectrum is only apparently higher by $\sqrt{3}$ because of its lower sampling, we see that the HRD-orbit exhibits a better noise characteristic than both kinematic orbits in the highest frequency range and still around the region of interest at $2 \cdot T_p$ = 60 s.

4.2 Fourier analysis of orbital velocities

As mentioned in section 3.3, gravity field recovery procedures like the energy integral method also require instantaneous orbital velocities as input data. This is the motivation to perform an analogue analysis for velocities as it was done in section 4.1 for positions. Note that orbital velocities are by-products of all types of HRD-orbits, which may be obtained by taking the time derivative of Eq. (2). For kinematic orbits, however, only approximate procedures can be applied to the kinematic positions like a 7-point Newton-Gregory interpolation proposed by Földváry *et al.* (2004).

Figure 6 shows amplitude spectra of orbital velocity differences over one day emerging from HRD-

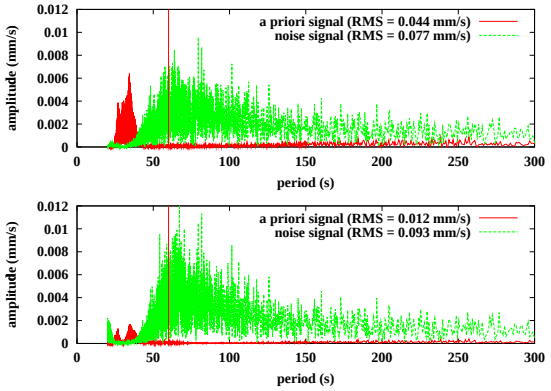

Fig. 6. Amplitude spectra due to noise and due to force model errors for HRD-orbit velocities based on pulses (top) and accelerations (bottom) with T_s = 10 s and T_p = 30 s.

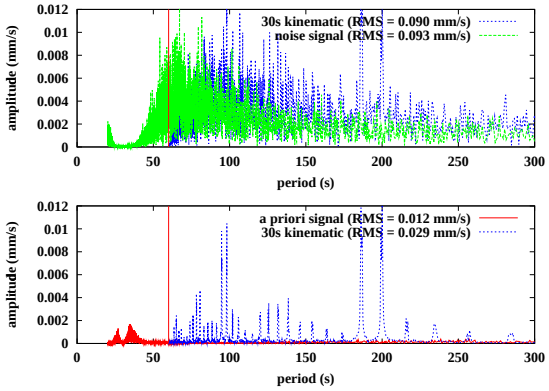

Fig. 7. Noise spectrum analogue to Fig. 6 (bottom) and total spectrum for 30 s kinematic velocities (top) and corresponding model error spectra (bottom).

orbits based on pulses (top) and accelerations (bottom), respectively, with T_s = 10 s and T_p = 30 s, i.e., spectra corresponding to the situation shown in Fig. 5 (bottom). Figure 6 (bottom) indicates for the acceleration-based velocities a negligible influence of the a priori gravity field signal in comparison with the noise level, at least over the considered one-day time interval (see section 4.3). The pulse-based velocities (top) show a similar picture if they are computed at the pulse epochs as the mean values of the left- and right-hand side limits of the discontinuous velocity vectors. Note that the stronger dependency on the a priori gravity field model favors acceleration-based velocities for the task of gravity field recovery. Comparing both noise spectra in Fig. 6 implies, on the other hand, that highly-resolved pulse-based solutions exhibit a more favorable noise reduction for the highest frequency range than the corresponding acceleration-based solutions, which was already observed in Table 1 for real data.

Figure 7 shows the amplitude spectra from Fig. 6 (bottom) amended by spectra of kinematic velocities, which were established by the Newton-Gregory interpolation from noise-free and noisy 30 s kinematic positions, respectively. Taking the apparently higher level of the last mentioned spectrum into account, we see similar noise for kinematic velocities and velocities from the acceleration based HRD-orbit, except for the highest frequency range. There, the performance of the kinematic velocities is better due to a more efficient smoothing of high frequency signals by the relatively long interpolation-intervals. Application of 60 s piecewise constant accelerations would lead to a similar effect for the HRD-solution. Note that comparable results would be obtained for the kinematic velocities if the same 7-point Newton-Gregory interpolation (30 s spacing between the positions used for interpolation) was applied to 10 s kinematic positions, but much worse results if the spacing of the used interpolation points was changed to 10 s.

Figure 7 (bottom) gives the corresponding noise-free spectra separately and shows that the Newton-Gregory interpolation introduces comparably large interpolation errors when compared to the HRD-spectrum, although the absolute errors do not exceed the level of 0.1 mm/s. The discrete spectral lines are not restricted to the period range shown in Fig. 7 (bottom), but continue to lower frequencies down to the orbital frequency. Figure 7 (top) shows that some of these lines even exceed the noise level of the total spectrum of the considered one day data set.

4.3 Impact of data accumulation

All gravity field recovery procedures make use of the accumulation of individual (daily) solutions in order to reduce random errors for a most reliable estimation of gravity field coefficients. Figure 8 illustrates for the most trivial error model how the HRD signal and noise spectra from Fig. 6 (bottom) would look if data had been accumulated over 400 days. It is simply assumed that all systematic errors are not reduced, which would be the (worst) case for a daily repeat orbit, whereas random errors are reduced by the square root of the number of accumulated solutions.

Figure 8 indicates that for long data sets the systematic errors would become more important than the random errors under the above mentioned assumptions, because the impact of the rather poor a priori force field (truncated at degree and order 20: right vertical line) starts to exceed the noise level in the lower frequency range. It remains to be seen whether such biases towards the a priori model would actually occur in real gravity recovery experiments. It is just as well possible that small systematic errors are reduced in a combination like random errors due to a permanently changing orbit geometry.

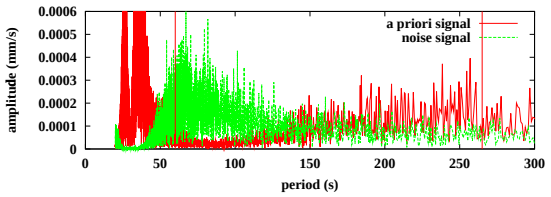

Fig. 8. Amplitude spectra from Fig. 6 (bottom). The noise spectrum is downscaled to simulate the worst case effect of data accumulation (see text).

To get an impression of the impact of the a priori model for real data, we repeated the processing described in section 3.3 with the gravity field model EGM96 (Lemoine *et al.*, 1997) instead of EIGEN-2 and compared the corresponding orbital velocities with each other. For the most interesting solution with T_s = 10 s and T_p = 30 s we found an overall RMS of velocity differences of 0.026 mm/s for pulses and 0.016 mm/s for accelerations due to the changed force model, which is comparable to the simulated results.

5 Conclusions

We presented a very efficient method to compute RD-orbits based on pseudo-stochastic parameters with resolutions $T_p \geq T_s$ and showed that MRD-orbits are, in essence, equivalent to kinematic orbits. The pre-processing of GPS data was found to be the most important aspect when generating the one-year data set of kinematic CHAMP positions. This problem is of course not removed when generating MRD-orbits.

An extensive simulation study showed that not only kinematic orbits but HRD-orbits, as well, could be interesting as input data for gravity field recovery, in particular for the upcoming GOCE mission (ESA, 1999) which is expected to provide 1 s GPS data. The influence of interpolation errors on kinematic velocities was found to be larger than the influence of the a priori gravity field model on HRD velocities, even if a very poor a priori model was used. First experiences gained with four weeks of real CHAMP GPS data confirmed, in essence, the expectations from the simulation study. However, the side-issue of generating most reliable 10 s GPS satellite clock corrections and the issue of a larger velocity noise level than expected from simulations for the acceleration-based HRD solutions need to be further studied.

References

Beutler G (2004) Methods of celestial mechanics. Springer, Berlin Heidelberg New York

Beutler G, Jäggi A, Hugentobler U, Mervart L (2005) Efficient orbit modelling using pseudo-stochastic parameters. J Geod (submitted)

European Space Agency ESA (1999) The Four Candidate Earth Explorer Core Missions: Gravity Field and Steady-State Ocean Circulation Mission. ESA SP-1233 (1)

Földváry L, Švehla D, Gerlach C, Wermuth M, Gruber T, Rummel R, Rothacher M, Frommknecht B, Peters T, Steigenberger P (2004) Gravity model TUM-2Sp based on the energy balance approach and kinematic CHAMP orbits. In: Reigber C, Lühr H, Schwintzer P, Wickert J (Eds) Earth observation with CHAMP, results from three years in orbit. Springer Verlag, Berlin Heidelberg New York, pp 13-18

Gerlach C, Földváry L, Švehla D, Gruber T, Wermuth M, Sneeuw N, Frommknecht B, Oberndorfer H, Peters T, Rothacher M, Rummel R, Steigenberger P (2003) A CHAMP-only gravity field model from kinematic orbits using the energy integral. Geophys Res Lett 30(20)

Hugentobler U, Schaer S, Fridez P (2001) Bernese GPS Software Version 4.2. Documentation, Astronomical Institute University of Berne

Jäggi A, Beutler G, Hugentobler U (2004a) Efficient stochastic orbit modeling techniques using least squares estimators. In: Sanso F (Ed) The proceedings of the international association of geodesy: a window on the future of geodesy. Springer, Berlin Heidelberg New York, pp 175-180

Jäggi A, Hugentobler U, Beutler G (2005) Pseudo-stochastic orbit modelling techniques for low Earth orbiters. J Geod (submitted)

Lemoine FG, Smith DE, Kunz L, Smith R, Pavlis EC, Pavlis NK, Klosko SM, Chinn DS, Torrence MH, Williamson RG, Cox CM, Rachlin KE, Wang YM, Kenyon SC, Salman R, Trimmer R, Rapp RH, Nerem RS (1997) The development of the NASA GSFC and NIMA Joint Geopotential Model. In: Segawa J, Fujimoto H, Okubo S (Eds) IAG Symposia: Gravity, Geoid and Marine Geodesy. Springer-Verlag, pp 461-469

Reigber C, Balmino G, Schwintzer P, Biancale R, Bode A, Lemoine JM, Koenig R, Loyer S, Neumayer H, Marty JC, Barthelmes F, Perosanz F, Zhu SY (2002) A high quality global gravity field model from CHAMP GPS tracking data and accelerometry (EIGEN-1S). Geophys Res Lett 29(14)

Reigber C, Schwintzer P, Neumayer KH, Barthelmes F, König R, Förste C, Balmino G, Biancale R, Lemoine JM, Loyer S, Bruinsma S, Perosanz F, Fayard T (2003) The CHAMP-only Earth Gravity Field Model EIGEN-2. Adv Space Res 31(8) 1883-1888

Švehla D, Rothacher M (2003) Kinematic and reduced-dynamic precise orbit determination of CHAMP satellite over one year using zero-differences, presented at EGS-AGU-EUG Joint Assembly, Nice, France

Švehla D, Rothacher M (2004) Kinematic precise orbit determination for gravity field determination. In: Sanso F (Ed) The proceedings of the international association of geodesy: a window on the future of geodesy. Springer, Berlin Heidelberg New York, pp 181-188

Touboul P, Willemenot E, Foulon B, Josselin V (1999) Accelerometers for CHAMP, GRACE and GOCE space missions: synergy and evolution. Boll Geof Teor Appl 40 321-327

Visser PNAM, Sneeuw N, Gerlach C (2003) Energy integral method for gravity field determination from satellite orbit coordinates. J Geod 77: 207-216

Wu SC, Yunck TP, Thornton CL (1991) Reduced-dynamic technique for precise orbit determination of low Earth satellites. J Guid, Control Dyn 14(1): 24-30